

## Selenotungstate Aggregates

Unprecedented Selenium and Lanthanide Simultaneously Bridging Selenotungstate Aggregates Stabilized by Four Tetra-vacant Dawson-like {Se<sub>2</sub>W<sub>14</sub>} UnitsHai-Lou Li,<sup>[a, b]</sup> Ya-Jie Liu,<sup>[a]</sup> Ya-Min Li,<sup>[a]</sup> Li-Juan Chen,<sup>\*[a]</sup> Jun-Wei Zhao,<sup>\*[a]</sup> and Guo-Yu Yang<sup>\*[b]</sup>

**Abstract:** In the presence of the larger [H<sub>2</sub>N(CH<sub>3</sub>)<sub>2</sub>]<sup>+</sup> and K<sup>+</sup> counter cations as structure-stabilizing agents, a class of unprecedented selenium and lanthanide (Ln) simultaneously bridging tetra-vacant Dawson-like selenotungstate aggregates [H<sub>2</sub>N(CH<sub>3</sub>)<sub>2</sub>]<sub>2</sub>Na<sub>9</sub>K<sub>2</sub>H<sub>19</sub>{[Ln<sub>4</sub>W<sub>4</sub>Se<sub>4</sub>O<sub>22</sub>(H<sub>2</sub>O)<sub>5</sub>](Se<sub>2</sub>W<sub>14</sub>O<sub>52</sub>)<sub>2</sub>}<sub>2</sub> · 60H<sub>2</sub>O [Ln = Tb<sup>III</sup> (1), Dy<sup>III</sup> (2), Ho<sup>III</sup> (3), Er<sup>III</sup> (4), Tm<sup>III</sup> (5), Yb<sup>III</sup> (6)] have been obtained by the one-pot assembly reaction of Na<sub>2</sub>WO<sub>4</sub> · 2H<sub>2</sub>O, Ln(NO<sub>3</sub>)<sub>3</sub> · 6H<sub>2</sub>O, and Na<sub>2</sub>SeO<sub>3</sub> under moderately acidic aqueous conditions and the complexes were structurally characterized by elemental analyses, IR spectra, single-crystal X-ray diffraction, powder X-ray diffraction (PXRD), and thermogravimetric (TG) analyses. It should be noted that the appropriate molar ratio of Se/W is extremely important in the formation of 1–6 and can effectively ameliorate the yield of 1–6. Moreover, dimethylamine hydrochloride is also indispensable and plays a considerably important role

in improving the solubility of Ln ions and stabilizing the structures of 1–6. The main polyoxoanion skeletons of 1–6 are constructed from two sandwich-type tetra-vacant Dawson-like {[Ln<sub>4</sub>W<sub>4</sub>Se<sub>4</sub>O<sub>22</sub>(H<sub>2</sub>O)<sub>5</sub>](Se<sub>2</sub>W<sub>14</sub>O<sub>52</sub>)<sub>2</sub>}<sup>16-</sup> half-units linked through two W-O-Ln bridges. The sandwich-type half-unit comprises two tetra-vacant Dawson-like [Se<sub>2</sub>W<sub>14</sub>O<sub>52</sub>]<sup>12-</sup> fragments encapsulating a unique dodecanuclear Se-Ln-W [Ln<sub>4</sub>W<sub>4</sub>Se<sub>4</sub>O<sub>22</sub>(H<sub>2</sub>O)<sub>5</sub>]<sup>8+</sup> oxo cluster. Their solid-state visible and NIR fluorescent properties and lifetime decay behaviors were measured and their solid-state luminescent spectra mainly demonstrate the characteristic emission bands of Ln<sup>3+</sup> ions. Moreover, the dominant wavelengths, the color purity, and correlated color temperatures of 1–5 have been also calculated. In addition, the luminous flux values of 1–5 are 2031, 6992, 3071, 921, and 477 lumen, respectively.

## Introduction


Polyoxometalates (POMs) are a well-known class of polynuclear anionic metal–oxygen clusters bearing unparalleled structural styles and fascinating features such as alterable shape, size, oxygen-rich surfaces, and high negative charge, which display diverse potential applications in the areas of catalysis, medicine, magnetism, gas sorption, molecular recognition, electronic materials, and nonlinear optics.<sup>[1]</sup> These potential applications of POMs have been painstakingly investigated because

the anionic cluster frameworks of POMs show several noticeable features: 1) they maintain high integrity in the solid state and in aqueous solution; 2) they display a wide range of well-defined sizes and a variety of shapes, often with highly symmetric topologies; 3) they possess interesting electronic properties (e.g., storage of various numbers of electrons without fundamental structure modification, leading to mixed-valence systems in which the extra electrons are extensively delocalized over the whole POM skeleton); and 4) they serve as multi-dentate inorganic ligands to incorporate either functional organic moieties or second metallic centers from the d and f blocks.<sup>[2]</sup>

Selenotungstates (STs) as an important subfamily of POMs that have attracted increasing interest in the past decade because of the enormous diversity of structures and potential applications. The past decade has witnessed great research developments in STs, including “pure” STs and different metals [such as transition metal (TM), (CH<sub>3</sub>)<sub>2</sub>Sn<sup>2+</sup>, and Ln] functionalized STs (Table S1 in the Supporting Information).<sup>[3–14]</sup> Some novel nano-sized “pure” ST clusters and TM-substituted STs were discovered by Cronin and co-workers in conventional acidic aqueous solution.<sup>[3–7]</sup> Kalinina et al. obtained a Mn-substituted dimeric ST in a template-driven reaction of Na<sub>2</sub>WO<sub>4</sub> · 2H<sub>2</sub>O with SeO<sub>2</sub> in the presence of MnCl<sub>2</sub> · 4H<sub>2</sub>O under acidic conditions.<sup>[8]</sup> Su’s group reported several Fe/Mn/(CH<sub>3</sub>)<sub>2</sub>Sn-substituted ST-based

[a] H.-L. Li, Y.-J. Liu, Y.-M. Li, Dr. L.-J. Chen, Prof. J.-W. Zhao  
Henan Key Laboratory of Polyoxometalate Chemistry, College of Chemistry  
and Chemical Engineering  
Henan University  
Kaifeng 475004 (China)  
E-mail: ljchen@henu.edu.cn  
zhaojunwei@henu.edu.cn

[b] H.-L. Li, Prof. G.-Y. Yang  
MOE Key Laboratory of Cluster Science, School of Chemistry  
Beijing Institute of Technology  
Beijing 100081 (China)  
E-mail: ygy@bit.edu.cn

 Supporting information and the ORCID identification number(s) for the author(s) of this article can be found under:  
<https://doi.org/10.1002/asia.201801010>

nanoclusters.<sup>[9–12]</sup> Furthermore, some research developments on Ln-containing STs (LnCSTs) have also been made because of the flexible and versatile combination between ST segments and Ln linkers. Among the reported LnCSTs, the Ce<sup>3+</sup>-incorporated STs are the most common.<sup>[13,14]</sup>

To the best of our knowledge, there is no report of selenium and Ln simultaneously bridging LnCST aggregates although numerous TM-, organotin-, and Ln-encapsulated STs and “pure” STs have been already obtained. This research background attracts our interest and provides us an excellent opportunity to explore this field. As our a part of our continuing work,<sup>[14,15]</sup> recently, we have concentrated on exploring the reaction system containing sodium tungstate, sodium selenite, and Ln nitrate in the presence of the larger charge-compensation cations [H<sub>2</sub>N(CH<sub>3</sub>)<sub>2</sub>]<sup>+</sup> and K<sup>+</sup> as structure-stabilizing agents to prepare novel selenium and Ln simultaneously bridging LnCST aggregates with previously unseen structures and interesting properties by the one-step synthetic strategy based on the following ideas: (a) because the SeO<sub>3</sub><sup>2-</sup> group has three highly active oxygen atoms aligned in the triangular pyramidal fashion and can readily combine with different metal ions, the SeO<sub>3</sub><sup>2-</sup> group should function as the bridging group to construct the {SeO<sub>3</sub>}<sup>-</sup> bridging LnCST aggregates, thus, to achieve this goal of triangular pyramidal {SeO<sub>3</sub>} groups as connectors in the structure construction, we will drastically increase the dosage of sodium selenite to enhance this possibility in the reaction process; (b) the lone electron pair stereochemical effect of the Se<sup>IV</sup> atom in the {SeO<sub>3</sub>} group is beneficial to create open-framework ST building blocks, which facilitates integration of oxophile active Ln ions and additional Se centers into unprecedented poly(LnCST) aggregates; (c) to stabilize the in situ formed poly(LnCST) polyoxoanions, larger charge-compensation cations, [H<sub>2</sub>N(CH<sub>3</sub>)<sub>2</sub>]<sup>+</sup> and K<sup>+</sup>, are simultaneously used in the reaction system. Herein, we report a family of selenium and Ln simultaneously bridging tetra-vacant Dawson-like heteropolyselenotungstate aggregates [H<sub>2</sub>N(CH<sub>3</sub>)<sub>2</sub>]<sub>2</sub>Na<sub>9</sub>K<sub>2</sub>H<sub>19</sub>{[Ln<sub>4</sub>W<sub>4</sub>Se<sub>4</sub>O<sub>22</sub>(H<sub>2</sub>O)<sub>5</sub>](Se<sub>2</sub>W<sub>14</sub>O<sub>52</sub>)<sub>2</sub>}<sub>2</sub> · 60H<sub>2</sub>O [Ln = Tb<sup>III</sup> (1), Dy<sup>III</sup> (2), Ho<sup>III</sup> (3), Er<sup>III</sup> (4), Tm<sup>III</sup> (5), Yb<sup>III</sup> (6)], the main polyoxoanion skeletons of which are assembled from two tetra-vacant Dawson-like {[Ln<sub>4</sub>W<sub>4</sub>Se<sub>4</sub>O<sub>22</sub>(H<sub>2</sub>O)<sub>5</sub>](Se<sub>2</sub>W<sub>14</sub>O<sub>52</sub>)<sub>2</sub>}<sup>16-</sup> sandwich-type units bridged by two W-O-Ln connectors. They represent the first {SeO<sub>3</sub>}-bridging LnCST aggregates stabilized by four tetra-vacant Dawson-like [Se<sub>2</sub>W<sub>14</sub>O<sub>52</sub>]<sup>12-</sup> units. Their solid-state luminescent properties and lifetime decay behaviors have been investigated at room temperature. Furthermore, the chromaticity coordinates of 1–5 have been indexed and the dominant wavelengths, color purities, and correlated color temperatures have also been calculated for them. The luminous flux values of 1–5 are also obtained.

## Results and Discussion

### Synthesis

In the past few decades, there have been numerous reports on “pure” STs and the metal functionalization of STs by TM, (CH<sub>3</sub>)<sub>2</sub>Sn<sup>2+</sup>, and Ln cations,<sup>[3–14]</sup> however, little work has been

devoted to the organic–inorganic composites with selenium and Ln simultaneously bridging LnCST aggregates. As a result, the elaborate design and preparation of novel triangular pyramidal {SeO<sub>3</sub>} bridging LnCST aggregates remains a huge challenge. The difficulties in manufacturing {SeO<sub>3</sub>} bridging LnCST aggregates lie in two factors: (i) as is well known to us, the direct combination of oxyphilic Ln ions with oxygen-rich lacunary ST fragments easily leads to amorphous precipitates instead of crystallization; (ii) LnCST fragments often have highly negatively charged surfaces, which means the introduction of negatively charged {SeO<sub>3</sub>} groups becomes more difficult. To overcome these difficulties, we utilized the assembly reaction of simple starting materials such as Na<sub>2</sub>WO<sub>4</sub> · 2H<sub>2</sub>O, Na<sub>2</sub>SeO<sub>3</sub>, and Ln(NO<sub>3</sub>)<sub>3</sub> · 6H<sub>2</sub>O under acidic conditions to cope with the first factor. In the meantime, we also increased the dosage of sodium selenite and introduced the larger charge-balancing [H<sub>2</sub>N(CH<sub>3</sub>)<sub>2</sub>]<sup>+</sup> and K<sup>+</sup> cations in the reaction process to deal with the second factor. Eventually, novel selenium and Ln simultaneously bridging tetra-vacant Dawson-like ST aggregates 1–6 were made by the one-pot reaction of Na<sub>2</sub>WO<sub>4</sub> · 2H<sub>2</sub>O, Na<sub>2</sub>SeO<sub>3</sub>, KCl, dimethylamine hydrochloride, and Ln(NO<sub>3</sub>)<sub>3</sub> · 6H<sub>2</sub>O in acidic aqueous medium. The results of parallel experiments reveal that a pH value in the range of 4.3–4.8 is all beneficial for the formation of 1–6. When the value is adjusted to 4.5 while keeping other conditions unchanged, their yields are the highest and their crystal shapes are perfect. Furthermore, we have also explored the effect of the molar ratio of Na<sub>2</sub>WO<sub>4</sub> · 2H<sub>2</sub>O/Na<sub>2</sub>SeO<sub>3</sub> on the formation of 1–6. In previous reports, the molar ratio of Se/W was varied in the range 0.06–0.70. We reported the lowest molar ratio of Se/W (0.06) in 2015,<sup>[14a]</sup> and the highest molar ratio of Se/W (0.70) was reported in 2010 by Cronin et al.<sup>[3]</sup> In this paper, we find when the molar ratio of Se/W varies in the range 1.40–2.50, 1–6 can be obtained, which is three times the reported highest ratio (0.70) and thirty-four times higher than the reported lowest ratio (0.06). Their yields of 1–6 are highest when the molar ratio of Se/W is 2.00. It should be pointed out that the Dawson-like ST [Se<sub>2</sub>W<sub>14</sub>O<sub>52</sub>]<sup>12-</sup> unit observed in 1–6 is relatively rare; it has been encountered during the course of preparing [(γ-Se<sub>2</sub>W<sub>14</sub>O<sub>52</sub>)<sub>3</sub>(Mo<sub>2</sub>O<sub>2</sub>(μ-S)<sub>2</sub>(H<sub>2</sub>O)<sub>2</sub>)<sub>6</sub>]<sup>124-</sup>, [(γ-Se<sub>2</sub>W<sub>14</sub>O<sub>52</sub>)<sub>4</sub>(WO<sub>3</sub>(H<sub>2</sub>O))<sub>8</sub>(W<sub>2</sub>O<sub>5</sub>)<sub>2</sub>(W<sub>4</sub>O<sub>12</sub>)<sub>2</sub>(Mo<sub>2</sub>O<sub>2</sub>(μ-S)<sub>2</sub>(H<sub>2</sub>O)<sub>2</sub>)<sub>4</sub>(Mo<sub>2</sub>O<sub>2</sub>(μ-S)<sub>2</sub>(SeO<sub>3</sub>))<sub>4</sub>]<sup>136-</sup>, and [H<sub>12</sub>Pd<sub>10</sub>Se<sub>10</sub>W<sub>52</sub>O<sub>206</sub>]<sup>128-</sup> in acidic media when using the simple WO<sub>4</sub><sup>2-</sup>/SeO<sub>2</sub>/SeO<sub>3</sub><sup>2-</sup> precursors and different metal entities.<sup>[7,16]</sup> In addition, by increasing the amount of heteroatoms, we previously reported a series of {AsO<sub>2</sub>(OH)} bridging Ln substituted arsenotungstates.<sup>[17]</sup> Apart from the above aspects, some efforts have been also put into explaining the influences of the usage of Ln cations in the reaction system. When the amount of Ln(NO<sub>3</sub>)<sub>3</sub> · 6H<sub>2</sub>O is changed from 0.12 g to 0.17 g, 1–6 can be afforded and their yields are the highest when the amount is adjusted to about 0.15 g. In addition, dimethylamine hydrochloride is indispensable and plays a considerably important role in improving the solubility of Ln ions and stabilizing the structures of the target products. If dimethylamine hydrochloride is absent, the reaction system will gradually become turbid during the course of stirring and lots of amorphous precipitation will be formed, and we cannot obtain 1–6. On the contrary, when dimethylamine hydrochloride is present, the reaction system re-



Figure 1. The simple synthetic process for obtain 1–6.

mains clear during the process of stirring and 1–6 will be successfully obtained (Figure 1).

### Structural description

The phase purity of the targeted samples have been characterized by the good agreement of the powder X-ray diffraction patterns with the simulated patterns derived from single-crystal X-ray diffraction (Figure S1 in the Supporting Information).

Single-crystal X-ray diffraction<sup>[18]</sup> reveals that 1–6 are isomorphous and crystallize in the triclinic space group  $P\bar{1}$ . Their polyoxoanionic skeletons contain a unique tetrameric entity of  $\{[\text{Ln}_4\text{W}_4\text{Se}_4\text{O}_{22}(\text{H}_2\text{O})_5](\text{Se}_2\text{W}_{14}\text{O}_{52})_2\}^{32-}$ . This tetrameric entity is constructed from four tetra-vacant Dawson-like  $[\text{Se}_2\text{W}_{14}\text{O}_{52}]^{12-}$  fragments and a previously unseen twenty-four-nuclear Se-Ln-W oxo cluster  $[\text{Ln}_4\text{W}_4\text{Se}_4\text{O}_{22}(\text{H}_2\text{O})_5]^{16+}$ . In accordance with the lanthanide contraction effect, the Ln–O bond lengths decrease as the ionic radius of the Ln cations decreases. Therefore, only the structure of 1 is described as an example below. The molecular structure of 1 consists of a tetrameric polyoxoanion  $\{[\text{Tb}_4\text{W}_4\text{Se}_4\text{O}_{22}(\text{H}_2\text{O})_5](\text{Se}_2\text{W}_{14}\text{O}_{52})_2\}^{32-}$  (1 a; Figure 2a and Figure S2 in the Supporting Information), nine  $\text{Na}^+$  cations, two

$[\text{H}_2\text{N}(\text{CH}_2)_2]^+$  cations, two  $\text{K}^+$  cations, nineteen protons, and sixty lattice water molecules. Bond valence sum (BVS) calculations indicate that the oxidation states of all W, Se, and Tb atoms are +6, +4, and +3, respectively (Table S2 in the Supporting Information).<sup>[19]</sup> In addition, terminal O5W and O4W linking to W1 and W16 can be also located by BVS calculations.<sup>[19]</sup> On one hand, 1 a can be described as a fusion of two equivalent dimeric  $\{[\text{Tb}_4\text{W}_4\text{Se}_4\text{O}_{22}(\text{H}_2\text{O})_5](\text{Se}_2\text{W}_{14}\text{O}_{52})_2\}^{16-}$  (1 b; Figure 2b) subunits linked by double W–O–Tb linkers. Subunit 1 b is built by two tetra-vacant Dawson-like  $[\text{Se}_2\text{W}_{14}\text{O}_{52}]^{12-}$  fragments sandwiching a previously unseen dodecanuclear Se–Tb–W  $[\text{Tb}_4\text{W}_4\text{Se}_4\text{O}_{22}(\text{H}_2\text{O})_5]^{8+}$  cluster (1 c; Figure 2c) through Tb–O–W, W–O–W, and Se–O–W linkers. The  $[\text{Se}_2\text{W}_{14}\text{O}_{52}]^{12-}$  fragment (Figure 2d) consists of eight tungsten centers in the equatorial position and two edge-sharing  $\{\text{W}_3\text{O}_{13}\}$  groups in two polar positions, in which each of the Se atoms is connected with a  $\mu_3$ -O atom and two  $\mu_2$ -O atoms to make the fragment more stable. The  $[\text{Se}_2\text{W}_{14}\text{O}_{52}]^{12-}$  fragment can be seen as removing a  $[\text{W}_4\text{O}_{10}(\text{H}_2\text{O})_2]^{4+}$  fragment from the  $[\text{Se}_2\text{W}_{18}\text{O}_{62}(\text{H}_2\text{O})_2]^{8-}$  cluster (Figure 2e).<sup>[13b]</sup> In fact, it is difficult to remove a  $[\text{W}_4\text{O}_8]^{8+}$  unit from the  $[\text{X}_2\text{W}_{18}\text{O}_{62}]^{6-}$  ( $\text{X} = \text{P}^{\text{V}}, \text{As}^{\text{V}}, \text{etc.}$ ) to form a tetra-vacant Dawson fragment (Figures S3 and S4 in the Supporting Infor-

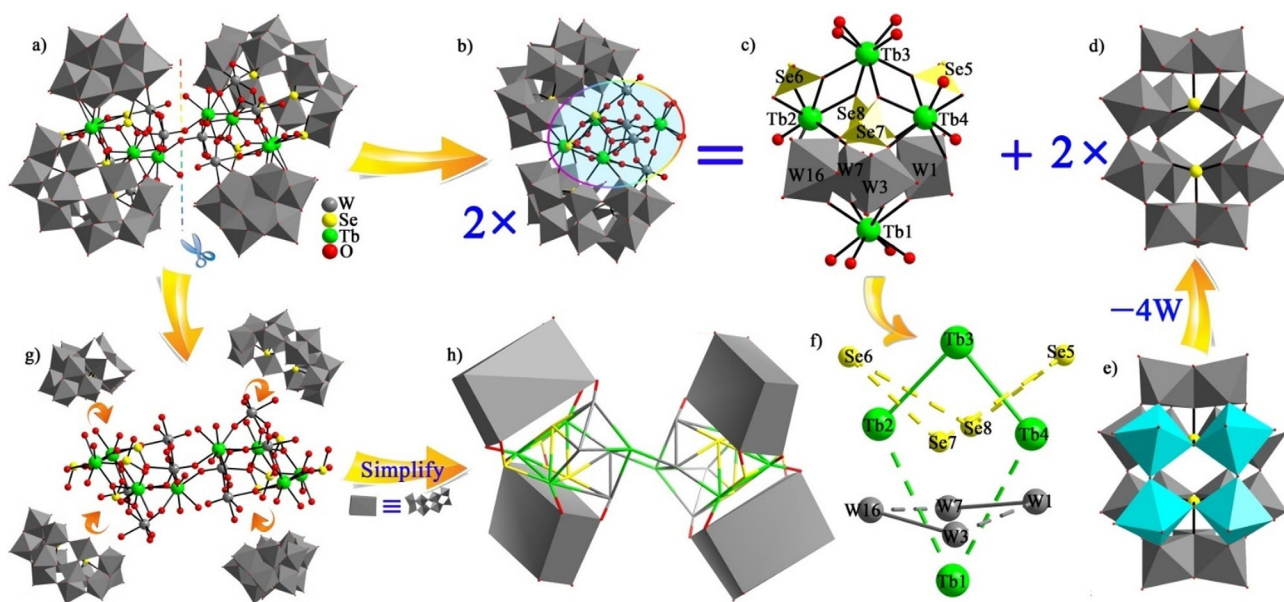


Figure 2. (a) The tetrameric polyoxoanion of 1 a. (b) The dimeric subunit of 1 b. (c) The dodecanuclear Se–Tb–W oxo cluster of 1 c. (d) The  $[\text{Se}_2\text{W}_{14}\text{O}_{52}]^{12-}$  fragment. (e) The  $[\text{Se}_2\text{W}_{18}\text{O}_{62}(\text{H}_2\text{O})_2]^{8-}$  precursor. (f) The alignment of four terbium atoms, four tungsten atoms, and four selenium atoms in 1 c. (g) Four  $[\text{Se}_2\text{W}_{14}\text{O}_{52}]^{12-}$  fragments in the quadrilateral motif around the twenty-four-nuclear Se–Tb–W oxo cluster  $[\text{Tb}_4\text{W}_4\text{Se}_4\text{O}_{22}(\text{H}_2\text{O})_5]^{16+}$ . (h) The simplified scheme of 1 a.

mation). We conjecture that there are three main reasons: (1) in the  $[\text{Se}_2\text{W}_{18}\text{O}_{62}(\text{H}_2\text{O})_2]^{8-}$  cluster, the  $[\text{W}_4\text{O}_{10}(\text{H}_2\text{O})_2]^{4+}$  fragment contains six terminal oxygen atoms and two coordination water ligands, thus weakening bonding force between the  $[\text{W}_4\text{O}_{10}(\text{H}_2\text{O})_2]^{4+}$  and the  $[\text{Se}_2\text{W}_{14}\text{O}_{52}]^{12-}$  fragment; (2) in the  $[\text{X}_2\text{W}_{18}\text{O}_{62}]^{6-}$  cluster, each heteroatom connects one  $\mu_2\text{-O}$  atom from the  $[\text{W}_4\text{O}_8]^{8+}$  fragment, so that the cluster is very difficult to decompose into the tetra-vacant Dawson fragment; (3) the lone-electron-pair stereochemical effect of the  $\text{Se}^{\text{III}}$  atom makes  $[\text{Se}_2\text{W}_{18}\text{O}_{62}(\text{H}_2\text{O})_2]^{8-}$  easier to form the tetra-vacant Dawson-like  $[\text{Se}_2\text{W}_{14}\text{O}_{52}]^{12-}$  building block. In **1**, the W–O bond lengths vary from 1.65(3) to 2.52(2) Å and the Se–O distances are between 1.677(18) and 1.75(2) Å. The previously unseen dodecanuclear cluster **1c** is extremely remarkable. It is built by four terbium atoms, four tungsten atoms, and four triangular  $\{\text{SeO}_3\}$  groups. In **1a**, the dodecanuclear cluster **1c** connects two tetra-vacant Dawson-like  $[\text{Se}_2\text{W}_{14}\text{O}_{52}]^{12-}$  fragments. Four  $\text{Tb}^{3+}$  cations in **1c** are in a quadrilateral plane (Figure 2f) and four  $\text{Tb}^{3+}$  cations are located on four vertices of the quadrilateral plane.  $\text{Tb}^{2+}$  and  $\text{Tb}^{3+}$  cations are connected with each other side by side and  $\text{Tb}^{3+}$  and  $\text{Tb}^{4+}$  are also linked to each other side by side, forming a horseshoe structure (Figure S5a in the Supporting Information).  $\text{Tb}^{2+}$  and  $\text{Tb}^{3+}$  cations are linked by two  $\mu_3\text{-O}$  atoms (O92, O56), whereas  $\text{Tb}^{3+}$  and  $\text{Tb}^{4+}$  cations are also linked by two  $\mu_3\text{-O}$  atoms (O10, O26; Figure S5a in the Supporting Information). It is most interesting that the  $\{\text{Se}_7\text{O}_3\}$  and  $\{\text{Se}_8\text{O}_3\}$  groups serve as connectors to link  $\text{Tb}^{2+}$ ,  $\text{Tb}^{3+}$ , and  $\text{Tb}^{4+}$  cations together, thus constructing the  $\{\text{Tb}_3\}$  cluster (Figure S5b in the Supporting Information). The  $\{\text{Se}_5\text{O}_3\}$  group not only joins the  $\text{Tb}^{3+}$  and  $\text{Tb}^{4+}$  cations through the O10 atom but also is connected with one  $[\text{Se}_2\text{W}_{14}\text{O}_{52}]^{12-}$  fragment through the O107 atom. Similarly, the  $\{\text{Se}_6\text{O}_3\}$  group combines  $\text{Tb}^{2+}$ ,  $\text{Tb}^{3+}$  cations and the other  $[\text{Se}_2\text{W}_{14}\text{O}_{52}]^{12-}$  fragment together through O92 and O88 atoms. Such special connection mode of the  $\{\text{SeO}_3\}$  groups linking Ln cations and POM fragments is unprecedented in coordination chemistry. Although there are four crystallographically independent  $\text{Tb}^{3+}$  ions in **1**, they exhibit an eight-coordinate distorted square antiprismatic geometry (Figure S6 in the Supporting Information). The square antiprismatic geometry of the  $\text{Tb}^{1+}$  ion is defined by five  $\mu_2\text{-O}$  atoms from  $\{\text{W}1\text{O}_6\}$ ,  $\{\text{W}3\text{O}_6\}$ ,  $\{\text{W}7\text{O}_6\}$ ,  $\{\text{W}16\text{O}_6\}$ , and  $\{\text{W}1\text{A}\text{O}_6\}$  octahedra [Tb–O: 2.33(2)–2.433(18) Å] and three water ligands [Tb–O: 2.44(2)–2.46(3) Å]. The square antiprismatic geometry of the  $\text{Tb}^{2+}$  ion is defined by two  $\mu_2\text{-O}$  atoms from one  $[\text{Se}_2\text{W}_{14}\text{O}_{52}]^{12-}$  fragment [Tb–O: 2.33(2)–2.34(2) Å], two  $\mu_2\text{-O}$  atoms, and four  $\mu_3\text{-O}$  atoms from **1c** [Tb–O: 2.31(2)–2.57(2) Å]. The square antiprismatic geometry of the  $\text{Tb}^{3+}$  ion is defined by four  $\mu_2\text{-O}$  atoms from two  $[\text{Se}_2\text{W}_{14}\text{O}_{52}]^{12-}$  fragments [Tb–O: 2.34(2)–2.42(2) Å] and four  $\mu_3\text{-O}$  atoms from **1c** [Tb–O: 2.377(18)–2.46(2) Å]. The square antiprismatic geometry of the  $\text{Tb}^{4+}$  ion is also constituted by two  $\mu_2\text{-O}$  atoms from the other  $[\text{Se}_2\text{W}_{14}\text{O}_{52}]^{12-}$  fragment [Tb–O: 2.287(19)–2.328(19) Å], two  $\mu_2\text{-O}$  atoms, and four  $\mu_3\text{-O}$  atoms from **1c** [Tb–O: 2.309(18)–2.638(19) Å]. Except for two  $[\text{Se}_2\text{W}_{14}\text{O}_{52}]^{12-}$  fragments, **1b** (Figure 2b) also contains four additional W centers (W1, W3, W7, W16) that play a very important bridging role in the structure construction. Specifically, the W3 atom

links to the terminal O98 atom [W–O: 1.70(2) Å], one  $[\text{Se}_2\text{W}_{14}\text{O}_{52}]^{12-}$  fragment through two  $\mu_2\text{-O}$  atoms [W–O: 1.79(2)–2.174(19) Å], the Se7 atom and the  $\text{Tb}^{4+}$  ion via one  $\mu_3\text{-O}$  atom [W–O: 2.28(2) Å], the W16 atom by one  $\mu_2\text{-O}$  atom [W–O: 1.94(2) Å], and the  $\text{Tb}^{1+}$  ion by one  $\mu_2\text{-O}$  atom [W–O: 1.763(19) Å]. The W16 atom is combined with the water ligand (O4W) [W–O: 2.278(19) Å], the terminal O16 atom [W–O: 1.78(3) Å], the  $\text{Tb}^{1+}$  ion by one  $\mu_2\text{-O}$  atom [W–O: 1.766(18) Å], the  $\text{Tb}^{2+}$  ion via one  $\mu_2\text{-O}$  atom and one  $\mu_3\text{-O}$  atom [W–O: 1.84(12)–2.31(2) Å], the Se7 atom by one  $\mu_3\text{-O}$  atom [W–O: 2.31(2) Å], and the W3 atom through one  $\mu_2\text{-O}$  atom [W–O: 1.96(2) Å]. The W7 atom joins to the terminal oxygen atom (O15) [W–O: 1.70(2) Å], the other  $[\text{Se}_2\text{W}_{14}\text{O}_{52}]^{12-}$  fragment via two  $\mu_2\text{-O}$  atoms [W–O: 1.999(19)–2.15(2) Å], the Se8 atom and  $\text{Tb}^{2+}$  ion through one  $\mu_3\text{-O}$  atom [W–O: 2.298(19) Å], the W1 atom by one  $\mu_2\text{-O}$  atom [W–O: 1.97(2) Å], and the  $\text{Tb}^{1+}$  ion by means of one  $\mu_2\text{-O}$  atom [W–O: 1.74(2) Å]. The W1 atom is connected with the water ligand (O5W) [W–O: 2.29(2) Å], three  $\text{Tb}^{3+}$  ( $\text{Tb}^{1+}$ ,  $\text{Tb}^{1+}$ ,  $\text{Tb}^{4+}$ , A:  $-x, -y, -z$ ) ions by three  $\mu_2\text{-O}$  atoms, and one  $\mu_3\text{-O}$  atom [W–O: 1.76(2)–2.21(2) Å], the Se8 atom through one  $\mu_3\text{-O}$  atom [W–O: 2.21(2) Å], and the W7 atom via one  $\mu_2\text{-O}$  atom [W–O: 1.999(19) Å].

Alternatively, **1a** can be perceived as four  $[\text{Se}_2\text{W}_{14}\text{O}_{52}]^{12-}$  fragments in a quadrilateral motif anchoring an unprecedented twenty-four-nuclear Se–Tb–W  $[\text{Tb}_4\text{W}_4\text{Se}_4\text{O}_{22}(\text{H}_2\text{O})_5]_2^{16+}$  cluster (Figure 2g). In the  $[\text{Tb}_4\text{W}_4\text{Se}_4\text{O}_{22}(\text{H}_2\text{O})_5]_2^{16+}$  cluster, two equivalent **1c** clusters are linked by two  $\mu_2\text{-O}$  atoms. To put it another way, **1a** can be understood as having two  $[\text{Se}_4\text{W}_{28}\text{Tb}_3\text{O}_{104}]^{15-}$  fragments (Figure S7a in the Supporting Information) that anchor one  $[\text{W}_8\text{Tb}_2\text{O}_{24}(\text{H}_2\text{O})_{10}]^{6+}$  group (Figure S7b in the Supporting Information), forming a unique tetrameric ST aggregate  $[\text{Se}_8\text{W}_{64}\text{Tb}_8\text{O}_{208}(\text{H}_2\text{O})_{10}]^{24-}$  (Figure S7c in the Supporting Information), and then eight extraneous  $\text{Se}^{\text{III}}$  atoms are incorporated into the ST aggregate and give rise to **1a** (Figure S7d in the Supporting Information). The 3D supramolecular packing alignments of **1** are illustrated in Figures S8 and S9 (in the Supporting Information).

As far as we know, such a structural feature in which four multi-vacant Dawson fragments are connected by TM or Ln cations is very rare in POM chemistry. It should be noted that the encapsulation mode of the multi-Se–Tb–W oxo cluster  $[\text{Tb}_4\text{W}_4\text{Se}_4\text{O}_{22}(\text{H}_2\text{O})_5]_2^{16+}$  in  $\{[\text{Tb}_4\text{W}_4\text{Se}_4\text{O}_{22}(\text{H}_2\text{O})_5][\text{Se}_2\text{W}_{14}\text{O}_{52}]_2\}^{32-}$  (Figure 3a) somewhat resembles that of the  $[\text{H}_{47}\text{WFe}_{27}\text{O}_{56}]^{22+}$   $\{\text{Fe}_{27}\}$  cluster in  $[\text{H}_{55}\text{P}_8\text{W}_{49}\text{Fe}_{27}\text{O}_{248}]^{26-}$  (**7**; Figure 3b) reported by Gouzerh et al.<sup>[20]</sup> It is not difficult to discover that several apparent structural differences between them are observed: (a) both multi-vacant POM building blocks are significantly different, the multi-vacant POM building block in **1** is the tetra-vacant Dawson-like  $[\text{Se}_2\text{W}_{14}\text{O}_{52}]^{12-}$  fragment whereas the multi-vacant POM building block in **7** is the hexa-vacant Dawson-type  $[\text{H}_2\text{P}_2\text{W}_{12}\text{O}_{48}]^{12-}$  fragment; (b) the intersection angles formed by two multi-vacant POM building blocks in the half-units of **1** and **7** are disparate, the intersection angle (54.44°) of the half-unit  $\{[\text{Tb}_4\text{W}_4\text{Se}_4\text{O}_{22}(\text{H}_2\text{O})_5][\text{Se}_2\text{W}_{14}\text{O}_{52}]_2\}^{16-}$  fragment (Figure 3c) in **1** is far larger than that (34.61°) of the half-unit  $[\text{H}_{27.5}\text{P}_4\text{W}_{24.5}\text{Fe}_{13.5}\text{O}_{124}]^{13-}$  cluster (Figure 3d) in **7**; (c) the chemi-

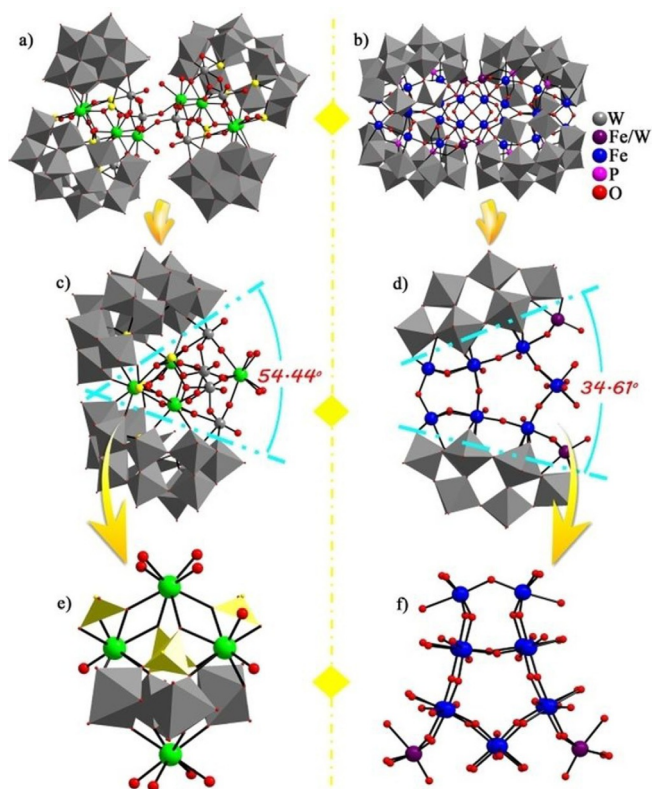


**Figure 3.** (a) The tetrameric polyoxoanion of **1**. (b) The tetrameric polyoxoanion of **7**. (c) The dimeric subunit  $[\text{Tb}_4\text{W}_4\text{Se}_4\text{O}_{22}(\text{H}_2\text{O})_5(\text{Se}_2\text{W}_{14}\text{O}_{52})_2]^{16-}$  in **1** highlighting the "bite" angle of  $54.44^\circ$ . (d) The dimeric subunit  $[\text{H}_{27.5}\text{P}_4\text{W}_{24.5}\text{Fe}_{13.5}\text{O}_{124}]^{13-}$  in **7** highlighting the "bite" angle of  $34.61^\circ$ . (e) The dodecanuclear Se-Tb-W oxo cluster  $[\text{Tb}_4\text{W}_4\text{Se}_4\text{O}_{22}(\text{H}_2\text{O})_5]^{8+}$  in **1**. (f) The tetradecanuclear Fe-W oxo cluster  $[\text{H}_{23.5}\text{W}_{0.5}\text{Fe}_{13.5}\text{O}_{28}]^{11+}$  in **7**.

cal components of two metal-oxo clusters located in the pockets of their tetrameric units are discrepant, the multi-nuclear  $[\text{Tb}_4\text{W}_4\text{Se}_4\text{O}_{22}(\text{H}_2\text{O})_5]^{8+}$  cluster in **1** is a dodecanuclear Se-Tb-W oxo cluster (Figure 3 e), however, the multi-nuclear  $[\text{H}_{23.5}\text{W}_{0.5}\text{Fe}_{13.5}\text{O}_{28}]^{11+}$  cluster in **7** is a tetradecanuclear Fe-W oxo cluster (Figure 3 f).

### Photoluminescence (PL) properties

Ln-based luminescent materials have attracted substantial interest because of the narrow emission lines and high color purity derived from transitions inside the 4f shell of the Ln ions,<sup>[21]</sup> as well as their wide applications in lighting and displays, biomarkers, drug carriers, photovoltaic devices (e.g., tunable lasers, light-emitting diodes (LEDs), amplifiers for optical communications and optical storage), and so on.<sup>[21,22]</sup> From the early application in lighting at the end of the 19th century to the appearance of the YAG:  $\text{Nd}^{3+}$  laser in 1964,<sup>[23]</sup> up to now, some inorganic metal-oxide luminescent materials such as  $\text{BaMgAl}_{10}\text{O}_{17}:\text{Eu}^{2+}$  and  $\text{GdMgB}_5\text{O}_{10}:\text{Ce}^{3+},\text{Tb}^{3+}$  have been commercially used to manufacture blue and green luminescent lamps, respectively.<sup>[24]</sup>

In general, Ln-based luminescent materials have aroused extensive interest owing to the electron energy levels of the 4f shells located inside the completely filled 5s and 5p subshells.

These outer completed shells protect the 4f electrons from the effects of the crystal field or similar effects. For this reason, the 4f electrons of  $\text{Ln}^{3+}$  ions can be placed in any of the 4f orbitals, which gives rise to many spectroscopic terms and energy levels.<sup>[25]</sup> As a result, apart from  $\text{La}^{3+}$  and  $\text{Lu}^{3+}$  ions, each Ln ion displays the characteristic intra 4f–4f transitions. Thus, the PL properties and lifetime decay behaviors of the solid-state samples of **1–6** have been investigated at room temperature. The visible solid-state emission spectra, excitation spectra, and the lifetime decay curves of **1–5** are illustrated in Figures S10 and S11 (in the Supporting Information). It can be seen explicitly that the emission spectra and excitation spectra of **1–5** all exhibit the characteristic peaks mainly derived from the  $\text{Ln}^{3+}$  ions. Because we have discussed the assignments of the characteristic peaks of these  $\text{Ln}^{3+}$  ions in our previous studies,<sup>[15,17]</sup> the related descriptions on the visible PL properties and lifetime decay behaviors of **1–5** are put in the Supporting Information. The lifetime decay curve of **1** under monitoring the most intense emission at 544 nm (Figure S10 b in the Supporting Information) is well fitted with a second-order exponential function, affording the lifetimes  $\tau_1$  and  $\tau_2$  being 1.20  $\mu\text{s}$  (9.95 %) and 12.80  $\mu\text{s}$  (90.05 %) and the average decay time being 11.64  $\mu\text{s}$ . Clearly, the average decay time ( $\tau^*$ ) of **1** is longer than that (5.29  $\mu\text{s}$ ) of the tetrameric tetra-Tb-incorporated tellurotungstate  $[\text{H}_2\text{N}(\text{CH}_3)_2]_6\text{H}_{12}\text{Na}_2\{\text{Sn}(\text{CH}_3)\text{W}_2\text{O}_4(\text{IN})\}[(\text{B}-\alpha\text{-TeW}_8\text{O}_{31})\text{Tb}(\text{H}_2\text{O})(\text{Ac})]_2 \cdot 25\text{H}_2\text{O}$ ,<sup>[15d]</sup> the main reason of which may be that the high frequency O–H oscillators of aqua ligands and the high frequency C–H oscillators of acetates around the  $\text{Tb}^{3+}$  ions in  $[\text{H}_2\text{N}(\text{CH}_3)_2]_6\text{H}_{12}\text{Na}_2\{\text{Sn}(\text{CH}_3)\text{W}_2\text{O}_4(\text{IN})\}[(\text{B}-\alpha\text{-TeW}_8\text{O}_{31})\text{Tb}(\text{H}_2\text{O})(\text{Ac})]_2 \cdot 25\text{H}_2\text{O}$  in some degree quench the luminescence emission and further lead to its shorter decay time.<sup>[26]</sup> In addition, the lifetime decay curves of **2–4** in the visible region also obey the second-order exponential function (Figure S10 d, f, h, j in the Supporting Information) and their  $\tau^*$  are 5.61  $\mu\text{s}$  for **2**, 5.72  $\mu\text{s}$  for **3**, and 4.69  $\mu\text{s}$  for **4**, which are very near to those (6.56  $\mu\text{s}$  for  $\text{Ln}=\text{Dy}^{\text{III}}$ , 6.07  $\mu\text{s}$  for  $\text{Ln}=\text{Ho}^{\text{III}}$ , 5.85  $\mu\text{s}$  for  $\text{Ln}=\text{Er}^{\text{III}}$ ) of our previously reported tetrameric tetra-Ln-incorporated arsenotungstates  $[\text{H}_2\text{N}(\text{CH}_3)_2]_6\text{Na}_6\text{H}_4\{\text{Ln}_4\text{W}_8\text{O}_{19}(\text{H}_2\text{O})_{10}(\text{OH})_2(\text{Ser})_2(\text{B}-\alpha\text{-AsW}_9\text{O}_{33})_4\} \cdot 38\text{H}_2\text{O}$  ( $\text{Ln}=\text{Dy}^{\text{III}}, \text{Ho}^{\text{III}}, \text{Er}^{\text{III}}$ ).<sup>[15c]</sup>

It can be found that the PL emissions of these compounds are mainly derived from the  $\text{Ln}^{3+}$  ions. However, there are still some differences in the PL properties between **1–5** and the corresponding  $\text{Ln}^{3+}$  nitrates, which may be attributed to the intramolecular energy transfer of the  $\text{O} \rightarrow \text{W}$  ligand-to-metal charge-transfer (LMCT) transitions, which can sensitize the emission of  $\text{Ln}^{3+}$  cations in **1–5** in the UV/Visible region.<sup>[27a,b]</sup> Therefore, further experiments have been conducted to confirm such intramolecular energy transfer in **1–5**. Owing to the simple energy state diagram with only one single emission band centered in the near-infrared region, the  $\text{Yb}^{3+}$  ion does not display luminescence emission in the UV/Visible region.<sup>[27c]</sup> Thus, the PL properties of **6** in the UV/Visible region mainly result from the  $\text{O} \rightarrow \text{W}$  charge-transfer transitions. Figure 4 a shows the PL excitation and emission spectra of **6**. By monitoring the emission at 455 nm of **6**, the excitation spectrum of **6** (Figure 4 a, left) reveals a sharp band with the maximum at 227 nm, which is assigned to the  $\text{O} \rightarrow \text{W} {}^1\text{A}_{1g} \rightarrow {}^1\text{T}_{1u}$  transitions

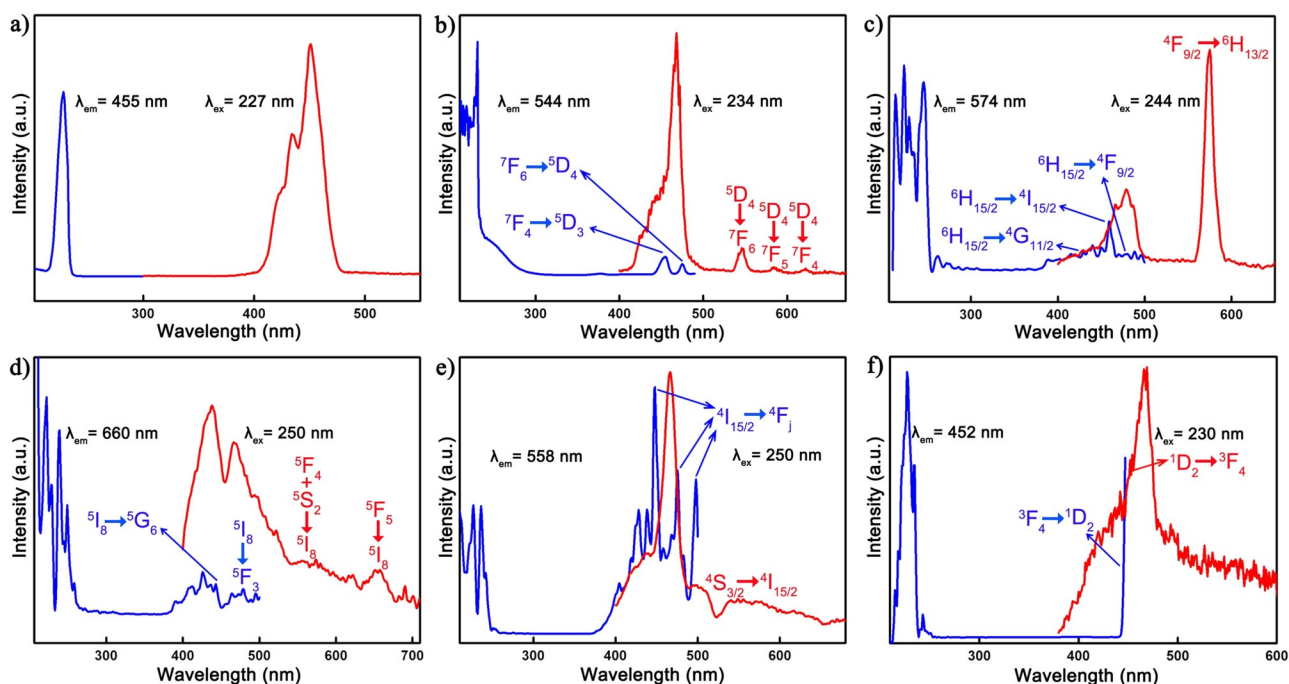


**Figure 4.** (a) The PL excitation spectrum and emission spectrum of **6**. (b) The PL excitation spectrum and emission spectrum of **1**. (c) The PL excitation spectrum and emission spectrum of **2**. (d) The PL excitation spectrum and emission spectrum of **3**. (e) The PL excitation spectrum and emission spectrum of **4**. (f) The PL excitation spectrum and emission spectrum of **5**.

of tungsten-oxygen cluster fragments.<sup>[27d]</sup> Upon the excitation at 227 nm (Figure 4a, right), **6** emits a broad emission band at 455 nm in the range 400–480 nm, which is induced by the  ${}^3T_{1u} \rightarrow {}^1A_{1g}$  transition derived from the excitation into the O→W LMCT band.<sup>[27a,b,d]</sup> Both excitation and emission peaks in **6** are ascribed to the O→W charge-transfer absorption in the tungsten-oxygen cluster fragments. Figure 4b–f show the excitation spectra and emission spectra of **1–5**, respectively. Their excitation spectra are collected by monitoring the corresponding emission of  $Ln^{3+}$  ions at 544 nm for **1**, 574 nm for **2**, 660 nm for **3**, 558 nm for **4**, and 452 nm for **5**. It can be clearly seen that all of the excitation spectra show a broad band in the range 210–260 nm derived from the  ${}^1A_{1g} \rightarrow {}^1T_{1u}$  transitions of the O→W LMCT band of the tungsten-oxygen cluster fragments as discussed above. In the range 390–500 nm in their excitation spectra, some excitation peaks assigned to the typical f–f transitions of  $Ln^{3+}$  ions can be observed, that is,  ${}^7F_4 \rightarrow {}^5D_3$  (454 nm),  ${}^7F_6 \rightarrow {}^5D_4$  (475 nm) for **1**,<sup>[28]</sup>  ${}^6H_{15/2} \rightarrow {}^4G_{11/2}$  (428 nm),  ${}^6H_{15/2} \rightarrow {}^4I_{15/2}$  (458 nm),  ${}^6H_{15/2} \rightarrow {}^4F_{9/2}$  (479 nm) for **2**,<sup>[15c]</sup>  ${}^5I_8 \rightarrow {}^5G_6$  (443 nm),  ${}^5I_8 \rightarrow {}^5F_3$  (478 nm) for **3**,  ${}^4I_{15/2} \rightarrow {}^4F_j$  (448 nm, 475 nm and 498 nm) for **4**,<sup>[29]</sup> and  ${}^3F_4 \rightarrow {}^1D_2$  (447 nm) for **5**.<sup>[30]</sup> Upon the excitation at 234 nm for **1**, 244 nm for **2**, 250 nm for **3**, 250 nm for **4**, and 230 nm for **5** from the oxygen-to-metal (O→W) charge-transfer transitions, their emission spectra all exhibit the emission band attributed to the  ${}^3T_{1u} \rightarrow {}^1A_{1g}$  transitions of tungsten-oxygen cluster fragments in the range 400–500 nm and some emission peaks associated with the transitions of  ${}^5D_4 \rightarrow {}^7F_6$  (546 nm),  ${}^5D_4 \rightarrow {}^7F_5$  (583 nm),  ${}^5D_4 \rightarrow {}^7F_4$  (621 nm) for **1**,  ${}^4F_{9/2} \rightarrow {}^6H_{13/2}$  (574 nm) for **2**,  ${}^5F_4 + {}^5S_2 \rightarrow {}^5I_8$  (554 nm),  ${}^5F_5 \rightarrow {}^5I_8$  (656 nm) for **3**,  ${}^4S_{3/2} \rightarrow {}^4I_{15/2}$  (556 nm) for **4**, and  ${}^1D_2 \rightarrow {}^3F_4$  (452 nm) for **5** of  $Ln^{3+}$  ions. We can clearly see from the com-

parisons between the excitation and emission spectra of **1–5** that the emission band attributed to the O→W LMCT transitions of tungsten-oxygen cluster fragments in their emission spectra can in some degree overlap with some emission peaks derived from the f–f transitions of  $Ln^{3+}$  ions in the corresponding excitation spectra, which indicate the existence of intramolecular energy transfer from tungsten-oxygen cluster fragments to the  $Ln^{3+}$  ions in **1–5**. In fact, the intramolecular energy transfer from the O→W LMCT triplet states to  $Eu^{3+}$  ions have been systematically studied by Yamase et al.<sup>[27d]</sup>

The NIR emission spectra and PL decay curves of the solid-state samples of **2**, **3**, **4**, and **6** have been also investigated at room temperature. Under excitation at 388 nm, the NIR emission spectrum of **2** consists of three weak and three clear characteristic emission bands of  $Dy^{3+}$  ions at 841 ( ${}^4F_{9/2} \rightarrow {}^6H_{7/2} + {}^6F_{9/2}$ ), 934 ( ${}^4F_{9/2} \rightarrow {}^6H_{5/2}$ ), 1003 ( ${}^4F_{9/2} \rightarrow {}^6F_{7/2}$ ), 1179 ( ${}^4F_{9/2} \rightarrow {}^6F_{5/2}$ ), 1291 ( ${}^6F_{11/2} + {}^6H_{9/2} \rightarrow {}^6H_{15/2}$ ), and 1391 nm ( ${}^4F_{9/2} \rightarrow {}^6F_{1/2}$ ) (Figure 5a).<sup>[31]</sup> The PL decay curve of **2** taken by monitoring the emission at 841 nm ( ${}^4F_{9/2} \rightarrow {}^6H_{7/2} + {}^6F_{9/2}$ ) can be well fitted to a second-order exponential function, the lifetimes  $\tau_1$  and  $\tau_2$  are 2.17  $\mu s$  (46.51%) and 10.08  $\mu s$  (53.49%), the pre-exponential factors  $A_1$  and  $A_2$  are 6410.21 and 1589.11, their average lifetime ( $\tau^*$ ) is calculated to be 6.40  $\mu s$  (Figure 5b). The NIR emission spectrum of **3** shows a strong peak at 977 nm and a weak peak at 1190 nm, which are, respectively, assigned to  ${}^5F_5 \rightarrow {}^5I_7$  and  ${}^5I_6 \rightarrow {}^5I_8$  transitions of the  $Ho^{3+}$  ion (Figure 5c).<sup>[32]</sup> The decay curve of **3** was monitored under the emission at 977 nm ( ${}^5F_5 \rightarrow {}^5I_7$ ) and excitation at 450 nm ( ${}^5I_8 \rightarrow {}^5G_6$ ), which can be well fitted into a second-order exponential function. The luminescence lifetimes  $\tau_1$  and  $\tau_2$  are 1.24  $\mu s$  (26.85%) and 12.55  $\mu s$  (73.15%), the pre-exponential factors  $A_1$  and  $A_2$  are 4159.92 and 1115.05, and

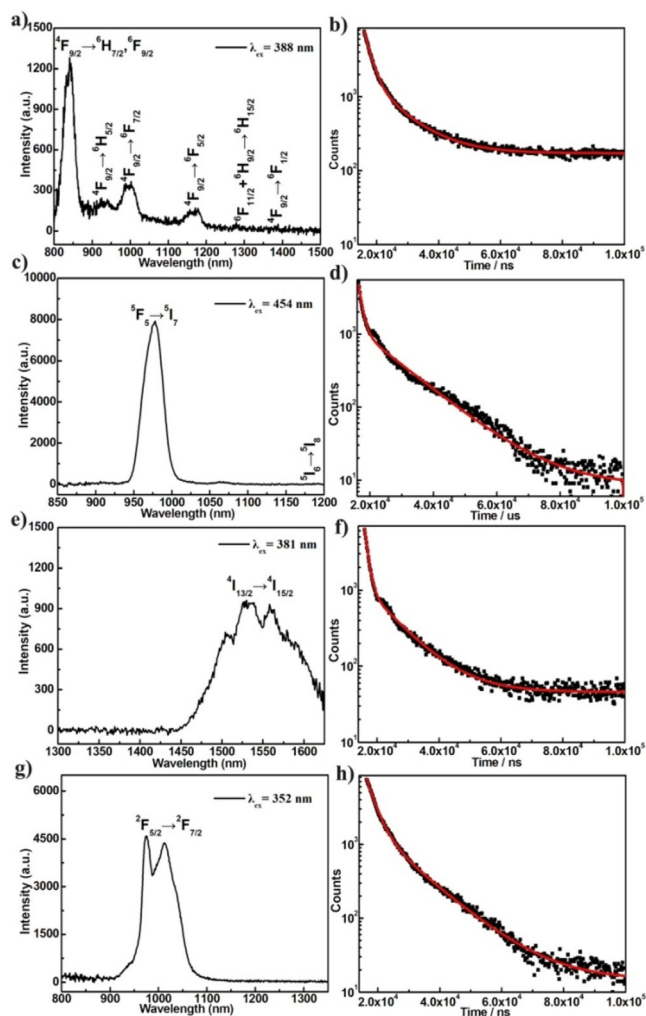


**Figure 5.** a) The NIR PL emission spectrum of **2**. b) The PL decay curve of **2** taken by monitoring the emission at 841 nm. c) The NIR PL emission spectrum of **3**. d) The PL decay curve of **3** taken by monitoring the emission at 977 nm. e) The NIR PL emission spectrum of **4**. f) The PL decay curve of **4** taken by monitoring the emission at 1536 nm. g) The NIR PL emission spectrum of **6**. h) The PL decay curve of **6** taken by monitoring the emission at 1012 nm.

their average lifetime is calculated to be 9.51  $\mu\text{s}$  (Figure 5d). The NIR emission spectrum of **4** shows a broad peak at 1536 nm, which is assigned to  $^4I_{13/2} \rightarrow ^4I_{15/2}$  transitions of the  $\text{Er}^{3+}$  ion (Figure 5e). The PL decay curve of the **4** can be well fitted into a second-order exponential function, the luminescence lifetimes  $\tau_1$  and  $\tau_2$  are 1.09  $\mu\text{s}$  (40.10%) and 9.71  $\mu\text{s}$  (59.30%), the pre-exponential factors  $A_1$  and  $A_2$  are 6395.01 and 1048.33, and the average lifetime is 6.20  $\mu\text{s}$  (Figure 5f). Furthermore, the lifetime decay curves of **2–4** in the NIR region also conform to the second-order exponential function. Their  $\tau^*$  values are 6.40  $\mu\text{s}$  for **2**, 9.51  $\mu\text{s}$  for **3**, and 6.20  $\mu\text{s}$  for **4**, and are also near to those (7.24  $\mu\text{s}$  for  $\text{Ln}=\text{Dy}^{\text{III}}$ , 5.92  $\mu\text{s}$  for  $\text{Ln}=\text{Ho}^{\text{III}}$ , 5.51  $\mu\text{s}$  for  $\text{Ln}=\text{Er}^{\text{III}}$ ) of our previously reported tetrameric tetra-Ln-incorporated arsenotungstates  $[\text{H}_2\text{N}(\text{CH}_3)_2]_6\text{Na}_6\text{H}_4[\text{Ln}_4\text{W}_8\text{O}_{19}(\text{H}_2\text{O})_{10}(\text{OH})_2(\text{Ser})_2(\text{B}-\alpha\text{-AsW}_9\text{O}_{33})_4] \cdot 38\text{H}_2\text{O}$  ( $\text{Ln}=\text{Dy}^{\text{III}}$ ,  $\text{Ho}^{\text{III}}$ ,  $\text{Er}^{\text{III}}$ ).<sup>[15c]</sup> With the excitation of 352 nm, the NIR spectrum of **6** exhibits an emission band with two split-

ting peaks at 973 and 1012 nm, which is assigned to the  $^2F_{5/2} \rightarrow ^2F_{7/2}$  transition of the  $\text{Yb}^{3+}$  ion (Figure 5g). The decay curve of the **6** can be well fitted into a second-order exponential function, the luminescence lifetimes  $\tau_1$  and  $\tau_2$  are 2.79  $\mu\text{s}$  (45.88%) and 12.15  $\mu\text{s}$  (54.12%), the pre-exponential factors  $A_1$  and  $A_2$  are 6350.27 and 1722.50, and the average lifetime is 7.86  $\mu\text{s}$  (Figure 5h).<sup>[33]</sup>

The CIE 1931 diagram is an internationally recognized useful approach for probing all the possible colors by combining three primary colors. The field of lighting and display devices refers to color in terms of the 1931 CIE chromatic color coordinates, which are one of the fundamental factors for evaluating performance.<sup>[34]</sup> It is very important that CIE coordinates and chromaticity diagram disclose the exact emission color and color purity of the sample.<sup>[35]</sup> Generally, all of the possible light source colors can be found at the only (x, y) coordinate in this color space. The CIE chromaticity coordinates for **1–5** are determined on the basis of their corresponding visible PL spectra and are indexed to (0.3703, 0.4516), (0.3914, 0.4381), (0.5124, 0.4671), (0.4664, 0.5154), and (0.2321, 0.2214), respectively (Figure 6).

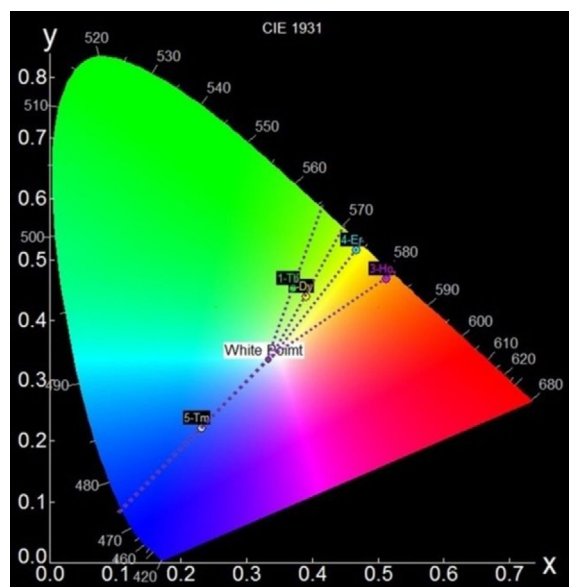


**Figure 6.** The CIE chromaticity diagram of the emissions of **1–5**.

The dominant wavelength can be defined as a monochromatic wavelength that appears to be the same color as the light source. On the CIE color coordinate space, a straight line drawn between the white point and the point for the color of the illuminant can be extrapolated out so that it intersects the perimeter of the space in two points. The point of intersection nearer to the color in question reveals the dominant wavelength of the color as the wavelength of the pure spectral color at that intersection point.<sup>[36]</sup> Furthermore, the color purity is the weighted average of the (x, y) coordinate relative to the coordinate of the illuminant and the coordinate of the dominant wavelength.<sup>[37]</sup> Thus, the color purity can be described by the following equation [Eq. (1)]:

$$\text{Color purity} = \frac{\sqrt{(x - x_i)^2 + (y - y_i)^2}}{\sqrt{(x_d - x_i)^2 + (y_d - y_i)^2}} * 100\% \quad (1)$$

The dominant wavelength of **1** is 566 nm. It is observed that the chromaticity coordinate (0.3703, 0.4516) is located in the yellowish and green region and the calculated color purity of **1** is found to be 47.19%. Usually the monochrome source is located on the perimeter of the chromaticity diagram, however, with white light the coordinates are located near the center of the chromaticity diagram. It is easy to see that the spectral band of **1** is a wide band, and the color coordinates color of **1** are close to the center of the chromaticity diagram. Similarly, the dominant wavelengths of **2–5** are 571, 582, 574, and 475 nm, respectively. In addition, the calculated color purity of **2–5** are found to be 48.97%, 93.95%, 94.67%, and 45.33%, respectively.

In addition, color temperature is a characteristic of visible light that has important applications in photography, videography, animal behavior, and other fields.<sup>[38]</sup> The color temperature of a light source can be defined as the temperature at which a black body would emit radiation of the same color as a given object. Thus, the color temperature can be described by the following equation [Eq (2)]:

$$T = 437n^3 + 3601n^2 - 6861n + 5514.31 \quad (2)$$

where  $n = (x - 0.3320)/(y - 0.1858)$ . The calculated color temperatures of **1–5** are found to be 4606 K, 4103 K, 2492 K, 3298 K, and 63 544 K, respectively.

Luminous flux refers to how the human eye can feel the radiation power, which is equal to the product of radiation energy per unit time of a band and relative visual rate of this band. As the human eye's relative visual rate is different for the different wavelengths of light, although the radiation power of different wavelengths of light is equal, the luminous flux is not equal. At present, owing to the prevalence of the LED industry, the luminous flux value is a main parameter to evaluate LED lighting.<sup>[39]</sup> Thus, the measured luminous flux values of **1–5** are 2031, 6992, 3071, 921, and 477 lumen, respectively.

## Conclusions

Six unprecedented selenium and Ln simultaneously bridging tetra-vacant Dawson-like ST aggregates  $[\text{H}_2\text{N}(\text{CH}_3)_2]_2\text{-Na}_9\text{K}_2\text{H}_{19}\{[\text{Ln}_4\text{W}_4\text{Se}_4\text{O}_{24}(\text{H}_2\text{O})_5](\text{Se}_2\text{W}_{14}\text{O}_{52})_2\}_2 \cdot 60\text{H}_2\text{O}$  [Ln = Tb<sup>III</sup> (**1**), Dy<sup>III</sup> (**2**), Ho<sup>III</sup> (**3**), Er<sup>III</sup> (**4**), Tm<sup>III</sup> (**5**), Yb<sup>III</sup> (**6**)] were successfully prepared by a one-pot self-assembly reaction and structurally characterized. Their tetrameric polyoxoanions  $\{[\text{Ln}_4\text{W}_4\text{Se}_4\text{O}_{22}(\text{H}_2\text{O})_5](\text{Se}_2\text{W}_{14}\text{O}_{52})_2\}^{32-}$  are constructed from four tetra-vacant Dawson-like  $[\text{Se}_2\text{W}_{14}\text{O}_{52}]^{12-}$  fragments and a twenty-four-nuclear Se-Ln-W oxo cluster  $[\text{Ln}_4\text{W}_4\text{Se}_4\text{O}_{22}(\text{H}_2\text{O})_5]^{16+}$ . We find that the molar ratio of Se/W, the pH value of the reaction system, the amount of Ln<sup>3+</sup> cations, and the participation of dimethylamine hydrochloride played important roles in the formation of **1–6**. Specifically, increasing the dosage of sodium selenite in the reaction system indeed provides the necessary condition for the

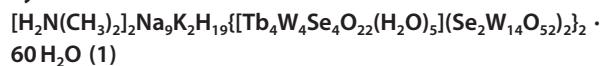
$[\text{SeO}_3]$  groups to act as connectors in the structure construction. Their solid-state visible and NIR PL properties and lifetime decay behaviors have been systematically studied. Furthermore, the dominant wavelength, the color purity, and correlated color temperatures of **1–5** have been calculated. In addition, the luminous flux values of **1–5** have been measured. In short, the successful synthesis of **1–6** not only demonstrates that increasing the dosage of sodium selenite in the one-step self-assembly reaction system to obtain selenium and Ln simultaneously bridging LnCST aggregates is feasible, but also can provide some useful guidance for constructing other heteroatom-participating (such as Sb<sup>III</sup>, Bi<sup>III</sup>, As<sup>III</sup>, and Te<sup>IV</sup>, etc.) Ln-incorporated POM aggregates.

## Experimental Section

### Materials and methods

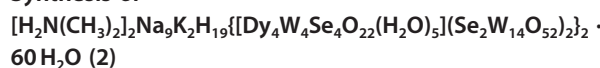
All used chemicals were commercially purchased without further purification. Elemental analyses were measured with a Vario EL Cube superuser V4.0.0 CHNS analyzer. IR spectra were collected from solid samples palletized with KBr with a PerkinElmer FTIR spectrometer between 400 and 4000 cm<sup>-1</sup>. Photoluminescence spectra and lifetime were recorded by using an FLS 980 Edinburgh Analytical Instrument apparatus equipped with a 450 W xenon lamp and a μF900H high-energy microsecond flashlamp as the excitation sources. TG analyses were performed under a N<sub>2</sub> atmosphere with a Mettler-Toledo TGA/SDTA 851<sup>e</sup> instrument with a heating rate of 10 °C min<sup>-1</sup> from 25 to 800 °C.

### Synthesis of



Na<sub>2</sub>WO<sub>4</sub> · 2 H<sub>2</sub>O (1.001 g, 3.035 mmol), Na<sub>2</sub>SeO<sub>3</sub> (1.002 g, 5.792 mmol), dimethylamine hydrochloride (0.501 g, 6.221 mmol), and KCl (0.501 g, 6.720 mmol) were dissolved in distilled water (30 mL) with stirring. The pH of the solution was adjusted to 5.4 by using HAC ( $V_{\text{HAC}}/V_{\text{H}_2\text{O}} = 1:1$ , 2.80 mL), and then the pH of the solution was adjusted to 4.5 by using HCl (6 mol L<sup>-1</sup>, 0.95 mL). After stirring for 20 min, Tb(NO<sub>3</sub>)<sub>3</sub> · 6 H<sub>2</sub>O (0.150 g, 0.331 mmol) was added and the pH of the solution was again adjusted to 4.5. The resulting solution was stirred for another 30 min and then filtered. Slow evaporation of the filtrate at ambient temperature led to the colorless prism crystals of **1** in about five weeks. Yield: 0.253 g (30.59%) based on Tb(NO<sub>3</sub>)<sub>3</sub> · 6 H<sub>2</sub>O. Elemental analyses calcd (%) for **1**: C 0.24, H 0.88, N 0.14; found: C 0.42, H 1.04, N 0.26; IR data:  $\tilde{\nu} = 3435, 3133, 2787, 1624, 1462, 954, 881, 830, 779, 483 \text{ cm}^{-1}$ .

### Synthesis of



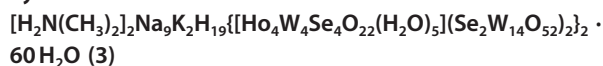
The synthetic procedure of **2** is similar to **1** except that Tb(NO<sub>3</sub>)<sub>3</sub> · 6 H<sub>2</sub>O was replaced by Dy(NO<sub>3</sub>)<sub>3</sub> · 6 H<sub>2</sub>O (0.152 g, 0.333 mmol). Colorless prism crystals of **2** were obtained. Yield: 0.214 g (25.68%) based on Dy(NO<sub>3</sub>)<sub>3</sub> · 6 H<sub>2</sub>O. Elemental analysis calcd (%) for **2**: C 0.24, H 0.88, N 0.14; found: C 0.38, H 1.00, N 0.22; IR data:  $\tilde{\nu} = 3443, 3152, 2787, 1624, 1462, 953, 889, 830, 779, 484 \text{ cm}^{-1}$ .



**Table 1.** Crystallographic data and structure refinements for 1–6.

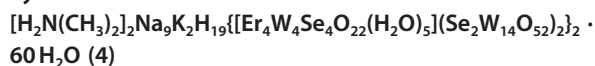
	1	2	3	4	5	6
Empirical formula	C <sub>4</sub> H <sub>175</sub> K <sub>2</sub> N <sub>2</sub> Na <sub>9</sub> O <sub>322</sub> Se <sub>16</sub> Tb <sub>8</sub> W <sub>64</sub>	C <sub>4</sub> H <sub>175</sub> K <sub>2</sub> N <sub>2</sub> Na <sub>9</sub> O <sub>322</sub> Se <sub>16</sub> Dy <sub>8</sub> W <sub>64</sub>	C <sub>4</sub> H <sub>175</sub> K <sub>2</sub> N <sub>2</sub> Na <sub>9</sub> O <sub>322</sub> Se <sub>16</sub> Ho <sub>8</sub> W <sub>64</sub>	C <sub>4</sub> H <sub>175</sub> K <sub>2</sub> N <sub>2</sub> Na <sub>9</sub> O <sub>322</sub> Se <sub>16</sub> Er <sub>8</sub> W <sub>64</sub>	C <sub>4</sub> H <sub>175</sub> K <sub>2</sub> N <sub>2</sub> Na <sub>9</sub> O <sub>322</sub> Se <sub>16</sub> Tm <sub>8</sub> W <sub>64</sub>	C <sub>4</sub> H <sub>175</sub> K <sub>2</sub> N <sub>2</sub> Na <sub>9</sub> O <sub>322</sub> Se <sub>16</sub> Yb <sub>8</sub> W <sub>64</sub>
F <sub>w</sub>	19990.69	20019.33	20038.77	20057.41	20070.77	20103.65
Crystal system	triclinic	triclinic	triclinic	triclinic	triclinic	triclinic
Space group	<i>P</i> $\bar{1}$	<i>P</i> $\bar{1}$	<i>P</i> $\bar{1}$	<i>P</i> $\bar{1}$	<i>P</i> $\bar{1}$	<i>P</i> $\bar{1}$
<i>a</i> [Å]	15.735(3)	15.6055(11)	15.404(10)	15.6535(19)	15.7311(12)	15.6438(15)
<i>b</i> [Å]	24.239(5)	23.1885(16)	23.690(15)	24.095(3)	23.1413(18)	23.130(2)
<i>c</i> [Å]	26.876(6)	26.6423(19)	26.147(18)	26.751(3)	26.661(2)	26.682(3)
$\alpha$ [°]	65.845(4)	68.1090(10)	65.850(12)	65.835(2)	68.0630(10)	68.464(2)
$\beta$ [°]	88.698(4)	87.9880(10)	88.877(13)	88.836(2)	87.704(2)	87.706(2)
$\gamma$ [°]	77.362(4)	71.3550(10)	77.504(12)	77.577(2)	71.1170(10)	70.955(2)
<i>V</i> [Å <sup>3</sup> ]	9101(3)	8437.5(10)	8475(10)	8964.2(19)	8482.2(11)	8454.0(14)
<i>Z</i>	1	1	1	1	1	1
$\mu$ [mm <sup>-1</sup> ]	23.396	25.329	25.322	24.046	25.526	25.725
<i>F</i> (000)	8726	8734	8742	8750	8758	8766
<i>T</i> [K]	296(2)	296(2)	296(2)	296(2)	296(2)	296(2)
Limiting indices	-18 ≤ <i>h</i> ≤ 18 -28 ≤ <i>k</i> ≤ 28 -31 ≤ <i>l</i> ≤ 30	-18 ≤ <i>h</i> ≤ 18 -27 ≤ <i>k</i> ≤ 22 -30 ≤ <i>l</i> ≤ 31	-18 ≤ <i>h</i> ≤ 18 -22 ≤ <i>k</i> ≤ 28 -25 ≤ <i>l</i> ≤ 31	-18 ≤ <i>h</i> ≤ 18 -28 ≤ <i>k</i> ≤ 27 -31 ≤ <i>l</i> ≤ 31	-18 ≤ <i>h</i> ≤ 18 -18 ≤ <i>k</i> ≤ 27 -31 ≤ <i>l</i> ≤ 31	-18 ≤ <i>h</i> ≤ 18 -27 ≤ <i>k</i> ≤ 25 -31 ≤ <i>l</i> ≤ 30
No. of reflections collected	46378	43146	42416	45648	43940	43570
No. of independent reflections	31594	29390	29084	31027	29681	29579
<i>R</i> <sub>int</sub>	0.0696	0.0749	0.0879	0.0629	0.0561	0.0715
Data/restraints/parameters	31594/266/1657	29390/386/1696	29084/284/1664	31027/236/1665	29681/288/1678	29579/325/1669
Goodness-of-fit on <i>F</i> <sup>2</sup>	1.037	1.045	1.025	1.023	1.032	1.034
Final <i>R</i> indices	<i>R</i> 1 = 0.0856 [ <i>I</i> > 2σ( <i>I</i> )] <i>wR</i> 2 = 0.1886	<i>R</i> 1 = 0.0767 <i>wR</i> 2 = 0.1733	<i>R</i> 1 = 0.0807 <i>wR</i> 2 = 0.1660	<i>R</i> 1 = 0.0714 <i>wR</i> 2 = 0.1565	<i>R</i> 1 = 0.0597 <i>wR</i> 2 = 0.1258	<i>R</i> 1 = 0.0787 <i>wR</i> 2 = 0.1882
<i>R</i> indices (all data)	<i>R</i> 1 = 0.1475 <i>wR</i> 2 = 0.2107	<i>R</i> 1 = 0.1304 <i>wR</i> 2 = 0.1914	<i>R</i> 1 = 0.1633 <i>wR</i> 2 = 0.1882	<i>R</i> 1 = 0.1205 <i>wR</i> 2 = 0.1737	<i>R</i> 1 = 0.1142 <i>wR</i> 2 = 0.1411	<i>R</i> 1 = 0.1417 <i>wR</i> 2 = 0.2115

### Synthesis of



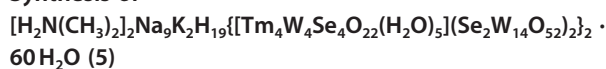
The synthetic procedure of **3** is similar to **1** except that Tb(NO<sub>3</sub>)<sub>3</sub> · 6H<sub>2</sub>O was replaced by Ho(NO<sub>3</sub>)<sub>3</sub> · 6H<sub>2</sub>O (0.151 g, 0.329 mmol). Pale-yellow prism crystals of **3** were obtained. Yield: 0.306 g (37.14%) based on Ho(NO<sub>3</sub>)<sub>3</sub> · 6H<sub>2</sub>O. Elemental analysis calcd (%) for **3**: C 0.24, H 0.88, N 0.14; found: C 0.34, H 0.97, N 0.25; IR data:  $\tilde{\nu}$  = 3457, 3155, 2796, 1631, 1464, 947, 896, 730, 773, 483 cm<sup>-1</sup>.

### Synthesis of



The synthetic procedure of **4** is similar to **1** except that Tb(NO<sub>3</sub>)<sub>3</sub> · 6H<sub>2</sub>O was replaced by Er(NO<sub>3</sub>)<sub>3</sub> · 6H<sub>2</sub>O (0.150 g, 0.325 mmol). Pink prism crystals of **4** were obtained. Yield: 0.247 g (30.28%) based on Er(NO<sub>3</sub>)<sub>3</sub> · 6H<sub>2</sub>O. Elemental analysis calcd (%) for **4**: C 0.24, H 0.88, N 0.14; found: C 0.40, H 1.05, N 0.22; IR data:  $\tilde{\nu}$  = 3434, 3140, 2780, 1624, 1470, 954, 889, 737, 779, 483 cm<sup>-1</sup>.

### Synthesis of



The synthetic procedure of **5** is similar to **1** except that Tb(NO<sub>3</sub>)<sub>3</sub> · 6H<sub>2</sub>O was replaced by Tm(NO<sub>3</sub>)<sub>3</sub> · 6H<sub>2</sub>O (0.149 g, 0.322 mmol).

Light-yellow prism crystals of **5** were obtained. Yield: 0.231 g (27.73%) based on Tm(NO<sub>3</sub>)<sub>3</sub> · 6H<sub>2</sub>O. Elemental analysis calcd (%) for **5**: C 0.24, H 0.88, N 0.14; found: C 0.35, H 1.08, N 0.22; IR data:  $\tilde{\nu}$  = 3442, 3141, 2780, 1624, 1462, 956, 895, 826, 781, 483 cm<sup>-1</sup>.

### Synthesis of



The synthetic procedure of **6** is similar to **1** except that Tb(NO<sub>3</sub>)<sub>3</sub> · 6H<sub>2</sub>O was replaced by Yb(NO<sub>3</sub>)<sub>3</sub> · 6H<sub>2</sub>O (0.154 g, 0.330 mmol). Colorless prism crystals of **6** were obtained. Yield: 0.198 g (23.90%) based on Yb(NO<sub>3</sub>)<sub>3</sub> · 6H<sub>2</sub>O. Elemental analysis (%) calcd for **6**: C 0.24, H 0.88, N 0.14; found: C 0.37, H 1.00, N 0.25; IR data:  $\tilde{\nu}$  = 3434, 3148, 2780, 1624, 1463, 962, 891, 822, 771, 483 cm<sup>-1</sup>.

### X-ray crystallography

Good single crystals of **1**, **2**, **3**, **4**, **5**, or **6** were prudentially picked under an optical microscope and sealed in a glass tube, which was closed at both ends. Their intensity data were collected with a Bruker APEX-II CCD detector at 296(2) K with Mo<sub>K $\alpha$</sub>  monochromated radiation ( $\lambda$  = 0.71073 Å). Direct methods were used to solve their structures and locate the heavy atoms by using the SHELXTL-97 program package.<sup>[16]</sup> The remaining atoms were found from successive full-matrix least-squares refinements on *F*<sup>2</sup> and Fourier syntheses. Lorentz polarization and SADABS corrections were applied. All hydrogen atoms attached to carbon and nitrogen atoms

were geometrically placed and refined isotropically as a riding model by using the default SHELXTL parameters. No hydrogen atoms associated with water molecules were located from the difference Fourier map. All non-hydrogen atoms were refined anisotropically except for some sodium, oxygen, nitrogen, and carbon atoms and water molecules. During the course of structural refinements, forty-four lattice water molecules for **1**, **3**, and **4** and forty lattice water molecules for **2**, **5**, and **6** per molecule were found from the Fourier maps. But, there are still solvent accessible voids in their check cif reports of crystal structures, indicating that some lattice water molecules should exist in the structures that cannot be found from the weak residual electron peaks. These water molecules are highly disordered and attempts to locate and refine them were unsuccessful. Based on elemental analyses and TG analyses, sixteen lattice water molecules for **1**, **3**, and **4** and twenty lattice water molecules for **2**, **5**, and **6** were directly added to each molecular formula. Crystallographic data and structural refinements for **1–6** are listed in Table 1. CCDC 1439023–1439028 contains the supplementary crystallographic data for this paper. These data can be obtained free of charge from The Cambridge Crystallographic Data Centre.

## Acknowledgments

This work was supported by the National Natural Science Foundation of China (21771052, 21671054, 21571048), the Innovation Scientists and Technicians Troop Construction Projects of Henan Province (174100510016), the Program for Science & Technology Innovation Talents in Universities of Henan Province (16HASTIT001), the Foundation of State Key Laboratory of Structural Chemistry (20160016), and the 2014 Special Foundation for Scientific Research Project of Henan University (XXJC20140001).

## Conflict of interest

The authors declare no conflict of interest.

**Keywords:** lanthanides · luminescent properties · polyoxometalates · selenotungstates · tetra-vacant Dawson structure

- [1] a) J. Marrot, M. A. Pilette, M. Haouas, S. Floquet, F. Taulelle, X. López, J. M. Poblet, E. Cadot, *J. Am. Chem. Soc.* **2012**, *134*, 1724–1737; b) Y. Zhao, D.-S. Deng, L.-F. Ma, B.-M. Ji, L.-Y. Wang, *Chem. Commun.* **2013**, *49*, 10299–10301; c) J. Heine, K. Müller-Buschbaum, *Chem. Soc. Rev.* **2013**, *42*, 9232–9242; d) A. B. Descalzo, R. Martínez-Mañez, F. Sancenón, K. Hoffmann, K. Rurack, *Angew. Chem. Int. Ed.* **2006**, *45*, 5924–5948; *Angew. Chem.* **2006**, *118*, 6068–6093; e) S.-T. Zheng, J. Zhang, X.-X. Li, W.-H. Fang, G.-Y. Yang, *J. Am. Chem. Soc.* **2010**, *132*, 15102–15103; f) B. Artetxe, S. Reinoso, L. S. Felices, L. Lezama, J. M. Gutiérrez-Zorrilla, J. A. García, J. R. Galán-Mascarós, A. Haider, U. Kortz, C. Vicent, *Chem. Eur. J.* **2014**, *20*, 12144–12156.
- [2] a) J. M. Clemente-Juan, E. Eugenio Coronado, A. Gaita-Ariño, *Chem. Soc. Rev.* **2012**, *41*, 7464–7478; b) D.-L. Long, R. Tsunashima, L. Cronin, *Angew. Chem. Int. Ed.* **2010**, *49*, 1736–1758; *Angew. Chem.* **2010**, *122*, 1780–1803; c) Y.-F. Song, R. Tsunashima, *Chem. Soc. Rev.* **2012**, *41*, 7384–7402.
- [3] J. Yan, D.-L. Long, L. Cronin, *Angew. Chem. Int. Ed.* **2010**, *49*, 4117–4120; *Angew. Chem.* **2010**, *122*, 4211–4214.
- [4] J. M. Cameron, J. Gao, L. Vilà-Nadal, D.-L. Long, L. Cronin, *Chem. Commun.* **2014**, *50*, 2155–2157.
- [5] J. Gao, J. Yan, S. Beeg, D.-L. Long, L. Cronin, *J. Am. Chem. Soc.* **2013**, *135*, 1796–1805.
- [6] J. Yan, J. Gao, D.-L. Long, H. N. Miras, L. Cronin, *J. Am. Chem. Soc.* **2010**, *132*, 11410–11411.
- [7] J. M. Cameron, J. Gao, D.-L. Long, L. Cronin, *Inorg. Chem. Front.* **2014**, *1*, 178–185.
- [8] I. V. Kalinina, E. V. Peresyphkina, N. V. Izarova, F. M. Nkala, U. Kortz, N. B. Kompankov, N. K. Moroz, M. N. Sokolov, *Inorg. Chem.* **2014**, *53*, 2076–2082.
- [9] W.-C. Chen, C. Qin, X.-L. Wang, Y.-G. Li, H.-Y. Zang, Y.-Q. Jiao, P. Huang, K.-Z. Shao, Z.-M. Su, E.-B. Wang, *Chem. Commun.* **2014**, *50*, 13265–13267.
- [10] W.-C. Chen, C. Qin, X.-L. Wang, K.-Z. Shao, Z.-M. Su, E.-B. Wang, *Cryst. Growth Des.* **2016**, *16*, 2481–2486.
- [11] W.-C. Chen, C. Qin, Y.-G. Li, H.-Y. Zang, K.-Z. Shao, Z.-M. Su, E.-B. Wang, H.-S. Liu, *Chem. Commun.* **2015**, *51*, 2433–2436.
- [12] W.-C. Chen, C. Qin, X.-L. Wang, C.-X. Wu, Y.-G. Li, H.-Y. Zang, K.-Z. Shao, Z.-M. Su, E.-B. Wang, *CrystEngComm* **2016**, *18*, 2820–2824.
- [13] a) W.-C. Chen, H.-L. Li, X.-L. Wang, K.-Z. Shao, Z.-M. Su, E.-B. Wang, *Chem. Eur. J.* **2013**, *19*, 11007–11015; b) W.-C. Chen, L.-K. Yan, C.-X. Wu, X.-L. Wang, K.-Z. Shao, Z.-M. Su, E.-B. Wang, *Cryst. Growth Des.* **2014**, *14*, 5099–5110.
- [14] a) H. L. Li, W. Yang, Y. Chai, L. J. Chen, J. W. Zhao, *Inorg. Chem. Commun.* **2015**, *56*, 35–40; b) Y. J. Liu, H. L. Li, C. T. Lu, P. J. Gong, X. Y. Ma, L. J. Chen, J. W. Zhao, *Cryst. Growth Des.* **2017**, *17*, 3917–3928.
- [15] a) J. Liu, H. Li, R. Zheng, Y. Liu, G. Jin, L. Chen, J. Zhao, *J. Solid State Chem.* **2017**, *256*, 196–202; b) Q. Han, Y. Wen, J.-C. Liu, W. Zhang, L.-J. Chen, J.-W. Zhao, *Inorg. Chem.* **2017**, *56*, 13228–13240; c) H.-L. Li, Y.-J. Liu, J.-L. Liu, L.-J. Chen, J.-W. Zhao, G.-Y. Yang, *Chem. Eur. J.* **2017**, *23*, 2673–2689; d) Q. Han, J.-C. Liu, Y. Wen, L.-J. Chen, J.-W. Zhao, G.-Y. Yang, *Inorg. Chem.* **2017**, *56*, 7257–7269.
- [16] M. A. Moussawi, S. Floquet, P. A. Abramov, C. Vicent, M. Haouas, E. Cadot, *Inorg. Chem.* **2018**, *57*, 56–63.
- [17] H. L. Li, Y. J. Liu, R. Zheng, L. J. Chen, J. W. Zhao, G. Y. Yang, *Inorg. Chem.* **2016**, *55*, 3881–3893.
- [18] a) G. M. Sheldrick, *SHELXL 97, Program for Crystal Structure Refinement*, University of Göttingen, Göttingen, Germany, **1997**; b) G. M. Sheldrick, *SHELXS 97, Program for Crystal Structure Solution*, University of Göttingen, Göttingen, Germany, **1997**.
- [19] I. D. Brown, D. Altermatt, *Acta Crystallogr. B* **1985**, *41*, 244–247.
- [20] B. Godin, Y.-G. Chen, J. Vaissermann, L. Ruhlmann, M. Verdagner, P. Gouzerh, *Angew. Chem. Int. Ed.* **2005**, *44*, 3072–3075; *Angew. Chem.* **2005**, *117*, 3132–3135.
- [21] a) C.-G. Ma, M. G. Brik, D.-X. Liu, B. Feng, Y. Tian, A. Suchocki, *J. Lumin.* **2016**, *170*, 369–374; b) E. G. Moore, A. P. S. Samuel, K. N. Raymond, *Acc. Chem. Res.* **2009**, *42*, 542–552.
- [22] a) J.-C. G. Bünzli, *Chem. Rev.* **2010**, *110*, 2729–2755; b) G. J. Sopsis, M. Orfanoudaki, P. Zampas, A. Philippidis, M. Siczek, T. Lis, J. R. O'Brien, C. J. Milios, *Inorg. Chem.* **2012**, *51*, 1170–1179.
- [23] J.-C. Bünzli, G. S. V. Eliseeva, *Chem. Sci.* **2013**, *4*, 1939–1949.
- [24] Y. J. Cui, Y. F. Yue, G. D. Qian, B. L. Chen, *Chem. Rev.* **2012**, *112*, 1126–1162.
- [25] F. Artizzu, M. L. Mercuri, A. Serpe, *Coord. Chem. Rev.* **2011**, *255*, 2514–2529.
- [26] C. Ritchie, V. Baslon, E. G. Moore, C. Reber, C. Boskovic, *Inorg. Chem.* **2012**, *51*, 1142–1151.
- [27] a) T. Yamase, M. Sugeta, *J. Chem. Soc. Dalton Trans.* **1993**, 759–765; b) T. Ito, H. Yashiro, T. Yamase, *Langmuir* **2006**, *22*, 2806–2810; c) H. Dong, S.-R. Du, X.-Y. Zheng, G.-M. Lyu, L.-D. Sun, L.-D. Li, P.-Z. Zhang, C. Zhang, C.-H. Yan, *Chem. Rev.* **2015**, *115*, 10725–10815; d) T. Yamase, *Chem. Rev.* **1998**, *98*, 307–325.
- [28] X. Fan, X. Xu, X. Yu, W. Chen, D. Zhou, J. Qiu, *Mater. Res. Bull.* **2018**, *99*, 398–402.
- [29] M. Back, E. Trave, R. Marin, N. Mazzucco, D. Cristofori, P. Riello, *J. Phys. Chem. C* **2014**, *118*, 30071–30078.
- [30] P. Alonso-Cristobal, O. Oton-Fernandez, D. Mendez-Gonzalez, J. F. Díaz, E. Lopez-Cabarcos, I. Barasoain, J. Rubio-Retama, *ACS Appl. Mater. Interfaces* **2015**, *7*, 14992–14999.
- [31] a) J. Feng, L. Zhou, S.-Y. Song, Z.-F. Li, W.-Q. Fan, L.-N. Sun, Y.-N. Yu, H.-J. Zhang, *Dalton Trans.* **2009**, 6593–6598; b) J. Feng, H.-J. Zhang, S.-Y.

- Song, Z.-F. Li, L.-N. Sun, Y. Xing, X.-M. Guo, *J. Lumin.* **2008**, *128*, 1957–1964.
- [32] S. Dang, J. B. Yu, X. F. Wang, L. N. Sun, R. P. Deng, J. Feng, W. Q. Fan, H. G. Zhang, *J. Lumin.* **2011**, *131*, 1857–1863.
- [33] W.-S. Lo, H. G. Li, G.-L. Law, W.-T. Wong, K.-L. Wong, *J. Lumin.* **2016**, *169*, 549–552.
- [34] T. Ghosh, E. Prasad, *J. Phys. Chem. C* **2015**, *119*, 2733–2742.
- [35] R. Yu, H. M. Noh, B. K. Moon, B. C. Choi, J. H. Jeong, H. S. Lee, K. Jang, S. S. Yi, *J. Lumin.* **2014**, *152*, 133–137.
- [36] K. Ji, Y. Xue, Z. Cui, *Opt. Mater.* **2015**, *47*, 180–184.
- [37] J. S. Kumar, K. Pavani, A. M. Babu, N. K. Giri, S. B. Rai, L. R. Moorthy, *J. Lumin.* **2010**, *130*, 1916–1923.
- [38] a) Q. Wang, H. S. Xu, F. Z. Zhang, Z. H. Wang, *Optik* **2017**, *129*, 21–29; b) A. Kapogiannatou, E. Paronis, K. Paschidis, A. Polissidis, N. G. Kostomitsopoulos, *Appl. Anim. Behav. Sci.* **2016**, *184*, 135–140.
- [39] a) C. Qian, X. J. Fan, J. J. Fan, C. A. Yuan, G. Q. Zhang, *Reliab. Eng. Syst. Safe* **2016**, *147*, 84–92; b) F. Haque, A. Azad, *Meas.* **2017**, *98*, 123–130.

---

Manuscript received: June 27, 2018

Accepted manuscript online: July 30, 2018

Version of record online: August 29, 2018

---